Metall. Res. Technol. **111**, 311–319 (2014)
© EDP Sciences, 2014
DOI: 10.1051/metal/2014016
www.metallurgical-research.org

&Metallurgical Research Technology

A 3D stochastic mesoscopic model for prediction of microstructure evolution during solidification of dendritic alloys

Laurentiu Nastac

The University of Alabama, Department of Metallurgical and Materials Engineering, Box 870202, Tuscaloosa, AL, 35487, USA
e-mail: lnastac@eng.ua.edu

Key words:
3D stochastic mesoscopic modeling; Casting; Solidification processing; Dendritic microstructure evolution; Segregation patterns

Received 22 December 2013
Accepted 25 March 2014

Abstract – A comprehensive three-dimensional (3D) stochastic model for simulating the evolution of dendritic crystals during the solidification of binary alloys was developed. The multi-scale model takes into account all the length scales (e.g., macro, micro- and meso-scales) required to accurately predict the evolution of dendritic morphologies during solidification of alloys. The model includes time-dependent computations for temperature distribution, solute redistribution in the liquid and solid phases, curvature, and growth anisotropy. Stochastic models previously developed for simulating dendritic grains in 2D were modified to control the nucleation and growth of dendrites in 3D. 3D mesoscopic computations at the dendrite tip length scale were performed to simulate the evolution of columnar and equiaxed dendritic morphologies including segregation patterns and compared then with predictions based on 2D mesoscopic computations.

A two-dimensional (2D) stochastic model has been proposed for the modelling of the evolution of dendritic morphologies during solidification [1]. The significance of the stochastic modeling approach is that the evolution of simulated micro- structures can be directly visualized and compared with the actual microstructures from experiments at two different scales: dendrite grain characteristics such as grain size and location and size of the columnar-to-equiaxed transition can be visualized at the meso-scale, while dendrite morphology (including dendrite tip, various dendrite arm spacings, microsegregation patterns) can be viewed at the microscale.

One of the challenges associated with stochastic modeling is reduction in mesh anisotropy. Basically, because of mesh anisotropy, dendrites will grow aligned with the axis of the mesh or at 45 degrees independently of the initial crystallographic orientation, which can be called anisotropy in growth direction. Furthermore, dendrites aligned with the axis would have narrower tips than predicted by classic theories, which can be termed anisotropy in growth kinetics. To reduce the mesh anisotropy, a formulation to correct the curvature in 2D was proposed and successfully validated [2]. A detailed discussion about correcting the grid anisotropy using the phase field approach is presented in [3].

Detailed comparison of predictions with measured microstructures requires the 2D stochastic model to be extended to 3D. This is why several 3D modelsfor simulating dendritic growth have been proposed in the literature including phase field approach [3, 4] and Lattice Boltzmann and Cellular Automaton approach [5]. To be efficient, these models require parallel computations and can be used only for relatively small domains. A 3D Cellular Automaton approach for modeling the evolution of dendritic grains has also been developed [6]. This 3D dendritic grain model is relatively fast but it cannot simulate the evolution of dendrites and of microsegregation patterns at the dendrite tip level. Thus, main goal of the current contribution is to develop an efficient 3D stochastic mesoscale dendritic growth model based on the previously developed 2D stochastic mesoscale dendritic growth model presented in [1]. The

https://doi.org/10.1051/metal/2014016 Published online by Cambridge University Press
Article published by EDP Sciences

3D model includes computations for temperature, solute, curvature and anisotropy at the dendrite tip level. Another goal of the paper is to compare the 2D and the 3D predictions in terms of microstructure evolution and segregation patterns.

The organization of this paper is as follows. The mathematical description of the 3D mesoscale stochastic model is presented in Section 2. The solution methodology is described in Section 3 and the algorithm in Section 4. In Section 5, the model is used to study the evolution of dendrite morphologies and of micro-segregation patterns in 3D and compared those with 2D predictions for a solidifying IN718 alloy

1 Mesoscale model for dendritic growth

The mathematical representation of the dendritic solidification process of a binary alloy is considered in a restricted 3D domain ($\boldsymbol{\Omega}$). A cross section of this 3D domain is shown in Figure 1. Here, $\vec{n}$ is the interface normal vector, $\bar{K}$ is the mean curvature of the interface, and the curve $\boldsymbol{\Gamma}$ represents the solid/liquid (S/L) interface which evolves in time and has to be found as part of the solution. The solidification of binary alloys is governed by the evolution of the temperature (T (x, y, z, t)) and concentration (C (x, y, z, t)) fields that have to satisfy several boundary conditions at the moving S/L interface as well as the imposed initial and boundary conditions on the computational domain. The equations that describe the physics of the solidification process in 3D Cartesian coordinates are as follows (see the 2D equations in [1,7–9]).

– Temperature (T) in $\boldsymbol{\Omega}$ (heat transfer equation):

$$\rho c_p \frac{\partial T}{\partial t} = \frac{\partial}{\partial x}\left(K\frac{\partial T}{\partial x}\right) + \frac{\partial}{\partial y}\left(K\frac{\partial T}{\partial y}\right) + \frac{\partial}{\partial z}\left(K\frac{\partial T}{\partial z}\right) - \rho L\frac{\partial f_L}{\partial t} \quad \text{with} \quad f_L = 1 - f_S \tag{1}$$

where t is time, ρ is the density, K is the thermal conductivity, c_p is the specific heat, L is the latent heat of solidification, f_L is the liquid fraction, f_S is the solid fraction, and x, y and z are the domain coordinates.

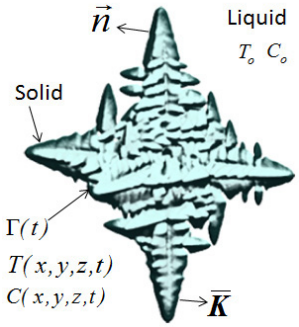


Fig. 1. A 3D-domain for dendritic solidification.

– Concentration (C) in $\boldsymbol{\Omega}$ (solute diffusion equation):

In the liquid phase (C_L):

$$\frac{\partial C_L}{\partial t} = \frac{\partial}{\partial x}\left(D_L\frac{\partial C_L}{\partial x}\right) + \frac{\partial}{\partial y}\left(D_L\frac{\partial C_L}{\partial y}\right) + \frac{\partial}{\partial z}\left(D_L\frac{\partial C_L}{\partial z}\right) \tag{2}$$

In the solid phase (C_S):

$$\frac{\partial C_S}{\partial t} = \frac{\partial}{\partial x}\left(D_S\frac{\partial C_S}{\partial x}\right) + \frac{\partial}{\partial y}\left(D_S\frac{\partial C_S}{\partial y}\right) + \frac{\partial}{\partial z}\left(D_S\frac{\partial C_S}{\partial z}\right) \tag{3}$$

where D_L and D_S are the interdiffusion coefficients in the liquid and solid, respectively.

Local equilibrium at the S/L interface on $\Gamma(t)$ (here, " * " means at interface):

$$C_S^* = kC_L^* \tag{4}$$

– Solute conservation at the S/L interface:

$$V_n^* C_L^* (k-1) = \left(-D_L\left(\frac{\partial C_L}{\partial x} + \frac{\partial C_L}{\partial y} + \frac{\partial C_L}{\partial z}\right) + D_S\left(\frac{\partial C_S}{\partial x} + \frac{\partial C_S}{\partial y} + \frac{\partial C_S}{\partial z}\right)\right)\vec{n} \tag{5}$$

where V_n^* is the normal velocity of the interface and $\vec{n}$ denotes the normal to the S/L interface that is pointing into the liquid (see Fig. 1).

– The interface temperature (T^*) is defined as (assuming local equilibrium with both phases):

$$T^* = T_L^{EQ} + \left(C_L^* - C_0\right)m_L - \Gamma\bar{\kappa}f(\varphi,\theta) \tag{6}$$

https://doi.org/10.1051/metal/2014016 Published online by Cambridge University Press

where T_L^{EQ} is the equilibrium liquidus temperature of the alloy, m_L is the liquidus slope of the phase diagram, $\bar{K}$ is the mean curvature of the S/L interface, Γ is the Gibbs-Thomson coefficient, and $f(\varphi, \theta)$ is a coefficient used to account for growth anisotropy where φ is the growth angle (i.e., the angle between the normal and the growth axis) and θ is the preferential crystallographic orientation angle.

In equation (6), second term in the right side is the constitutional undercooling and the last term in the right side is the curvature undercooling (that reduces the total undercooling at the dendrite tip, that is, has a stabilizing effect on the S/L interface). The interface temperature is also affected by the kinetic undercooling. The kinetic undercooling is not accounted for in this model since its effect becomes significant only at very high solidification velocities (i.e., in the rapid solidification regime). Also, the coefficient $f(\varphi, \theta)$ in equation (6) assumes an axisymmetric approximation where the anisotropy and the interface shape are independent of the polar angle ϕ in the x-y plane perpendicular to the growth axis [3].

2 Solution methodology

The solidification process is governed by equations (1) to (6) and a stochastic model for nucleation and growth. The numerical procedures for calculating the nucleation and growth, temperature and concentration fields as well as the growth velocity of the S/L interface are described in details below.

2.1 Stochastic model for nucleation and growth

The structure of the stochastic model is similar to that described in reference [10]. It consists of a regular network of cells that resembles the geometry of interest. The model is characterized by (a) geometry of the cell; (b) state of the cell; (c) neighborhood configuration; and (d) several transition rules that determine the state of the cell. In this work, the geometry of the cell is a cube. Each cell has three possible states: "liquid", "interface", or "solid". The selected neighborhood configuration is based on the cubic von Neumann's definition of neighborhood, that is the first order configuration and it contains the first six nearest neighbors. Solidification behavior depends to a great extent on the transition rules. In this model, the change of state of the cells from "liquid" to "interface" to "solid" is initiated either by nucleation or by growth of the dendrites.

At the beginning of the simulation, all cells are liquid, and their state index is set to zero. As nucleation proceeds, some cells become "interface" cells, and their index is changed to an integer larger than zero, n. The cells in contact with the mold wall are identified with a different reference index, m. The index is transferred from the parent cell to adjacent cells, as they become "solid" cells through growth. The integer accounts for the preferential growth of cubic crystals in the ⟨100⟩ direction. For graphical representation, each integer has a color associated with it, and each cell is a pixel on the computer screen. Both crystallographic orientation and random location of the new dendrites are chosen randomly among 256 orientation classes that are the first 256 colors used for graphical representation. The probability, $dp(\theta)$, that a newly nucleated dendrite has a principal growth direction in the range $[\theta_i, \theta_i + d\theta_i]$ is given by

$$dp(\theta) = \frac{2}{\pi} d\theta_i \quad \text{with} \quad \frac{2}{\pi} \int_{-\pi/4}^{\pi/4} dp(\theta) = 1 \tag{7}$$

where $2/\pi$ takes into account the four-fold symmetry of the cubic crystal (see integral in Eq. (7)). Note that in the case of the current 3D calculations, the θ_i are the angles between the normal n and the two local principal directions on the boundary.

The number of equiaxed and columnar dendrites, ∂N_e and ∂N_c, that can nucleate in the volume of the liquid and at the surfaces (boundaries) of the mold (computational domain) during one time step, δt, is calculated by using the nucleation site distributions, $N_e(\Delta T)$ and $N_c(\Delta T)$, respectively. Thus, assuming no solid movement in the liquid, nucleation rate is given by [10]:

$$\frac{\partial N}{\partial t} = -2\,\mu_N\,(\Delta T)\,\frac{\partial T}{\partial t}\,(1 - f_S) \tag{8}$$

https://doi.org/10.1051/metal/2014016 Published online by Cambridge University Press

where N is the number of nuclei, ΔT is the bulk undercooling, and μ_N is a nucleation parameter. The nucleation probabilities for "liquid" cells located in the bulk of the liquid and at the surface of the mold (dp_e and dp_c) to nucleate during each time step are given by

$$dp_e = \frac{\partial N_e}{N^v - N^s} \quad \text{and} \quad dp_c = \frac{\partial N_c}{N^s} \tag{9}$$

where N^v and N^s are the number of cells in the bulk and at the mold surface, respectively. During the time step calculation both the mold-surface cells and bulk cells are scanned and a random number, *rand*, is generated for each of them ($0 \leqslant rand \leqslant 1$). The nucleation of a "liquid" cell will occur only if $rand \leqslant dp_e$ or $rand \leqslant dp_c$.

It is assumed that a nucleus formed at a particular location will grow based on the growth velocity of the S/L interface given by equation (5) and the neighborhood configuration rule previously described. As nucleation succeeds, a nucleated "liquid" cell will become an active "interface" cell (e.g., n or $m > 0$), and will grow until its solid fraction becomes one. Thereafter, the "interface" cell would capture the neighboring cells if a randomly generated number, *rand*, is smaller than the capture probability, p_c, defined as follows:

$$p_c = \frac{1}{\sqrt{\tan^2 \theta_i + 1}} \tag{10}$$

where θ_i angles between the normal n and the two local principal directions on the boundar take values from $-\pi/4$ to π /4. At the capturing time, the state index of the "interface" cell is transferred to the captured neighboring cells that will become "interface" cells. Then, the "interface" cell becomes a "solid" cell. Further, the same procedure is used until all "liquid" or "interface"cells become "solid" cells.

2.2 Calculation of the temperature field

An implicit finite difference scheme (based on the successive over-relaxation method) is used to calculate the temperature of each cell as described by equation (1). This scheme does not impose any restriction on the time step used in calculations. An initial temperature higher than the equilibrium melting temperature of the alloy was assigned for all cells and convective boundary conditions (through the use of surface heat transfer coefficients) were used for surface cells.

2.3 Calculation of the time step

Time step used in calculations is given by

$$\delta t = \frac{1}{5}\min\left(\frac{a}{V_{\max}}, \frac{a^2}{D_L}, \frac{a^2}{D_S}\right) \tag{11}$$

where a is the mesh size (uniform in x, y, and z directions) and $V_{\max}$ is the maximum growth velocity obtained by scanning the growth velocities (V_n^*) of all "interface" cells during each time-step (see Eq. (12)). Equation (11) satisfies the conditions for both the explicit tracking scheme of the moving S/L interface and for explicitly calculating the concentration fields in both the solid and liquid phases.

2.4 Calculation of the concentration fields in the liquid and solid phases

An explicit finite difference scheme is used for calculating the concentration fields in the liquid and solid phases. This scheme is stable for the time-step condition shown in equation (11). Zero-flux boundary conditions were used for cells located at the surface of the geometry. The solution algorithm includes the "interface" cells by multiplying the concentration in the liquid by the liquid fraction and the concentration in the solid by the solid fraction of the particular interface cell. Also, during each time-step calculation and for each "interface" cell, the previous values of the liquid and solid concentrations are updated to the current values of the interface liquid and solid concentrations calculated with equations (4), (5), and (12) to (15).

2.5 Calculation of the growth velocity of the S/L interface

For "interface" cells, the values of the interface velocities in the x, y, and z directions are obtained from equations (4) and (5). For V_x

https://doi.org/10.1051/metal/2014016 Published online by Cambridge University Press

the finite difference form is as follows (similar for V_y and V_z):

$$V_x(i,j,k) = \frac{D_L}{a(1-k)}\left[\left(1-\frac{C_L(i-1,j,k)}{C_L^*(i,j,k)}\right) \times f_L(i-1,j,k) + \left(1-\frac{C_L(i+1,j,k)}{C_L^*(i,j,k)}\right) f_L(i+1,j,k)\right] + \frac{kD_S}{a(1-k)}\left[\left(1-\frac{C_S(i-1,j,k)}{kC_L^*(i,j,k)}\right) \times f_S(i-1,j,k) + \left(1-\frac{C_S(i+1,j,k)}{kC_L^*(i,j,k)}\right) f_S(i+1,j,k)\right] \quad (12)$$

2.6 Calculation of the fraction of solid evolution

Knowing the velocity components in x, y, and z directions, the solid fraction increment is calculated with:

$$\delta f_S = \frac{\delta t}{a}\left(V_x + V_y + V_z - V_x V_y \frac{\delta t}{a} - V_x V_z \frac{\delta t}{a} - V_z V_y \frac{\delta t}{a}\right) \quad (13)$$

Then, the solid fraction and growth velocity (V_n^*) are computed based on equation (13) as:

$$f_s^n = f_S^o + \delta f_S \quad \text{and} \quad V_n^* = \delta f_S \frac{a}{\delta t} \quad (14)$$

where superscripts "n" and "o" denote new and old solid fraction values, respectively.

2.7 Calculation of the interface liquid concentration

C_L^* is calculated from equation (6) as

$$C_L^* = C_O + \frac{\left(T^* - T_L^{EQ} + \Gamma \bar{K} f(\phi,\theta)\right)}{m_L} \quad (15)$$

The procedures for calculating $\bar{K}$ and $f(\varphi,\theta)$ are described below.

2.8 Calculation of the Interface Curvature

The average interface curvature for a cell with the solid fraction f_S is calculated with the following expression:

$$\bar{K} = \frac{1}{a}\left(1 - 2\frac{f_S + \sum_{k=1}^{N} f_S(k)}{N+1}\right) \quad (16)$$

where N is the number of neighboring cells. In the present 3D calculations, $N = 26$, that contains all the first order neighboring cells (including diagonal cells). Equation (16) is a simple counting-cell technique that approximates the mean geometrical curvature (and not the local geometrical curvature). The values of the curvatures calculated with equation (16) vary from a maximum of $1/a$ to zero for convex surfaces and from zero to a minimum of $-1/a$ for concave surfaces.

The curvature can also be computed with [9,11]:

$$\bar{K} = -(\nabla \hat{n}) = \frac{1}{|\vec{n}|}\left[\left(\frac{\vec{n}}{|\vec{n}|}\nabla\right)|\vec{n}| - (\nabla \vec{n})\right] \quad (17)$$

where the unit normal $\hat{n}$, $\hat{n} = \frac{\vec{n}}{|\vec{n}|}$, is derived from a normal vector $\vec{n}$, $\vec{n} = \nabla f_S$, which is the gradient of f_S. Thus, the 3D curvature in non-conservative form can be rewritten as [12]:

$$\bar{K} = -\frac{1}{\left((f_S)_x^2 + (f_S)_y^2 + (f_S)_z^2\right)^{3/2}} \times \left[(f_S)_{xx}\left((f_S)_y^2 + (f_S)_z^2\right) + (f_S)_{yy}\left((f_S)_x^2 + (f_S)_z^2\right) + (f_S)_{zz} \times \left((f_S)_x^2 + (f_S)_y^2\right) - 2(f_S)_x (f_S)_y (f_S)_{xy} - 2(f_S)_x (f_S)_z (f_S)_{xz} - 2(f_S)_z (f_S)_y (f_S)_{zy}\right] \quad (18)$$

where the partial derivatives of f_S are computed using centered finite difference approximations. $\bar{\kappa}$ is computed from the first 26 neighboring cells only at gridpoints adjacent to the S/L interface.

https://doi.org/10.1051/metal/2014016 Published online by Cambridge University Press

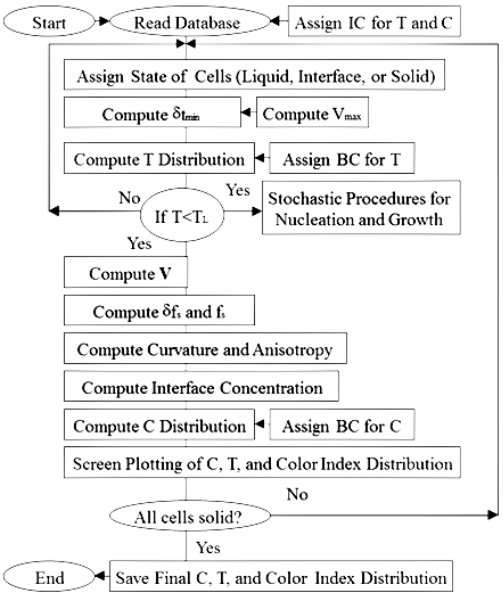


Fig. 2. Flowchart of the stochastic model.

2.9 Calculation of the anisotropy

The anisotropy of the surface tension (see Eq. (6)) is calculated as [3]:

$$f(\varphi, \theta) = 1 + \frac{4\delta}{1-3\delta}\left(\cos^4(\varphi-\theta) + \frac{3}{4}\sin^4(\varphi-\theta)\right)$$

with

$$\varphi = a\cos\left(\frac{V_z}{\left[(V_x)^2 + \left(V_y\right)^2 + (V_z)^2\right]^{1/2}}\right) \quad (19)$$

where φ is the angle between the normal direction to the solid-liquid interface and the [10] direction (growth axis), θ is calculated with equation (7) and δ accounts for the degree of anisotropy. For cubic symmetry, $\delta = 0.047$ [3]. Equation (19) again assumes an axisymmetric approximation where the anisotropy and the interface shape are independent of the polar angle ϕ in the x-y plane perpendicular to the growth axis [3].

3 Algorithm

The flowchart for the stochastic model is presented in Figure 2, where T is the new temperature distribution, T_L is the equilibrium liquidus temperature of the alloy, C and the new concentration distribution, $\delta t_{\min}$ is the current time step used in calculations, and IC and BC stand for initial and boundary conditions. The simulation software was written in Visual Fortran 90. The output of the model consists of screen plotting at any chosen time of C, T, or color indexes of all cells. Also, the final values of C, T, and color indexes of all cells are saved at the end of computations on the computer disk.

4 Results and discussion

Thermo-physical properties of the alloys used in simulations are presented in Table 1. The IN718-5 wt. % Nb alloy is considered to be a pseudo-binary alloy [9,13]. The grid size of both the 2×4 mm 2D domain and the $2\times4\times1$ mm 3D domain is $a = 5$ μm. This grid size is fine enough to approximately resolve the dendrite tip radius that, in the present solidification conditions, is larger than 5 μm. The average interface curvature is computed with equation (16). Newton cooling boundary condition was applied only to the bottom of the computational domain. All the other boundaries were assumed to be perfectly insulated. The surface heat transfer coefficient used in the present simulations is $h = 10^3$ W m^{-2} K^{-1}. Zero-flux solute boundary conditions were applied at the boundaries of the computational domain (i.e., a closed system was assumed). The initial melt temperature was assumed to be 1400 °C. Also, an initial concentration equal to C_o was assumed everywhere on the computational domain.

In Figure 3, a comparison of 2D ((a) and (b)) and 3D ((c) and (d)) simulated microstructures and segregation patterns (columnar dendritic morphologies) in unidirectional solidification of IN718-5 wt. % Nb alloy is illustrated. The 3D results are taken from the middle of the thickness of the simulated domain. The 2D computations were done by using the 2D stochastic dendritic model presented in [1,7–9]. The competition between nucleation and growth of multiple columnar dendrites is evident in both 2D and 3D cases. The strong growth competition from the sample bottom (>20 dendrites)

https://doi.org/10.1051/metal/2014016 Published online by Cambridge University Press

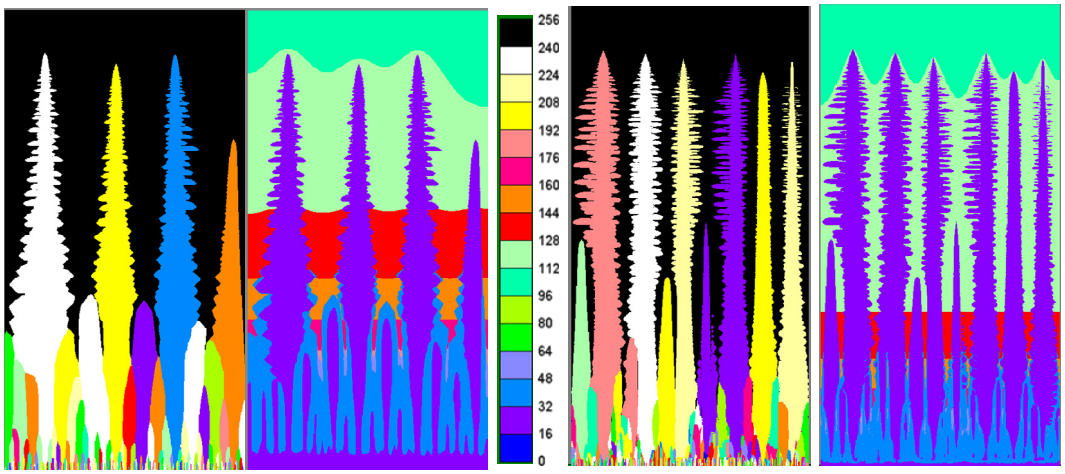


Fig. 3. Comparison of 2D ((a) and (b)) and 3D ((c) and (d)) simulated columnar dendritic morphologies and segregation patterns in unidirectional solidification of IN718-5 wt.% Nb alloy.

Table 1. Thermophysical properties of IN718-5Nb used in simulations [9, 13].

Property	μ_N^C [m^{-2} K^{-2}]	μ_N^E [m^{-3} K^{-2}]	L [J/kg]	ρ [kg/m^3]	K [W/m/K]	c_p [J/kg/K]	T_L [°C]
Value	1×10^6	5×10^8	2.9×10^5	7620	30.1	720	1336
Property	C_o [wt.%]	C_{eut} [wt.%]	k_o –	D_L [m^2 s^{-1}]	D_S [m^2 s^{-1}]	m_L [°C %$^{-1}$]	Γ [K m]
Value	5.0	19.1	0.48	3×10^{-9}	1×10^{-12}	–10.5	3.65×10^{-7}

to 1/4 of the sample height (10 dendrites) to 1/3 of the sample height (6 dendrites in 2D and 9 dendrites in 3D) to 2/3 of the sample height (4 dendrites in 2D and 6 dendrites in 3D) can be observed. Also, for 3D computations, more dendrites are observed toward the top of the sample, which is because more nucleation sites are available in 3D than in 2D and also because some dendrites that are visualized are cut from a different plane. The segregation patterns are also different in 3D when compared with 2D simulations, namely, the segregation profile in the upward direction is higher in 2D than in 3D.

Note also that the columnar morphologies are different in 3D than in 2D. This is because for a 2D geometry the grain growth is confined in the x-y plane while for the 3D case the grain growth can is free in the third (z) direction.

The Nb segregation index (SI) shown in the legend in Figure 3 is computed as follows:

$$SI = \frac{C_{av} - k^* C_o}{C_{eut} - k^* C_o} * 255$$

with

$$C_{av} = C_S f_S + C_L f_L$$

The legend in Figure 3 also shows the 256 color indexes (CI varies from 0 to 255) (legend displays 16 classes, where each class contains 16 different color indexes) used for displaying the preferential crystallographic orientation angle. The orientation angles can be extracted from the legend using the following equation: $\theta_i = \pi/2 * (CI/255) - \pi/4$. Thus, when $CI/255$ varies from 0 to 1, θ_i ranges from $-\pi/4$ to $\pi/4$.

Figure 4 shows a comparison between 2D and 3D computations in terms of equiaxed dendritic morphologies. The equiaxed grain density was $f \times 10^8$ nuclei/m^2 in 2D and 10^{12} nuclei/m^2 in 3D. The conversion factor

https://doi.org/10.1051/metal/2014016 Published online by Cambridge University Press

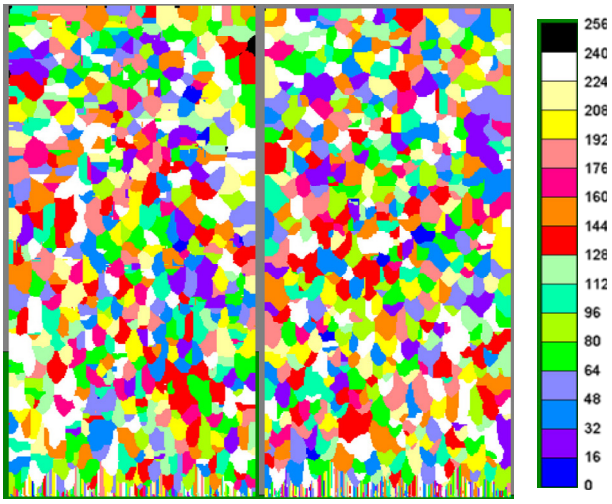


Fig. 4. Comparison of 2D (a) and 3D (b) simulated equiaxed dendritic morphologies in unidirectional solidification of IN718-5 wt.% Nb alloy.

$f = \pi/4$ [14]. Similar equiaxed morphologies can be observed from Figure 4 for both 2D and 3D cases, implying that 2D computations can be used and then the grain size can be converted to 3D by using the "$1/f$" conversion factor.

A RAM memory size of 100 bytes/cell is needed in the present 3D computations. CPU-time is related to the domain size and the time-step (Eq. (11)) and, for the simulation problems presented in Figures 3 and 4, is of the order of few hours on a Dell Precision T7500 desktop.

5 Conclusions and future work

The following conclusions can be drawn:

(i) an efficient 3D mesoscale stochastic model was developed in this work. The model can be used to simulate 3D microstructures using PCs (one microprocessor) with reasonable amount of RAM and CPU time and therefore no parallel computations are needed;
(ii) it was observed that based on the current simulations that the 3D columnar dendritic morphologies look different than the 2D columnar dendritic morphologies; this is because (1) for a 2D geometry the grain growth is confined in the x-y plane while for the 3D case it is free in the third (z) direction; (2) more nucleation sites are available in 3D than in 2D and (3) some dendrites that are visualized in the middle plane of the 3D simulation are cut from a different plane.
(iii) However, the 3D equiaxed dendritic morphologies appear to be similar with 2D equiaxed dendritic morphologies. Consequently, a simple conversion factor ($4/\pi$) can be used to convert the 2D grain size to 3D grain size.

Future work will include the following modelling aspects:

(i) correction of the mesh anisotropy [2,3];
(ii) improvement in the calculation of the interface curvature by including all the first and second order neighboring cells [1,9] as well as equation (18);
(iii) fluid flow study (3D case): the effects of the fluid flow on the microstructure evolution for a 3D geometry can be analyzed properly; this could not be done for a 2D geometry;
(iv) columnar-to-equiaxed transition (CET) will be modelled and analysed in details in the near future and compared with experimental observations.

References

[1] L. Nastac, *Acta Materialia* **47** (1999) 4253-4262
[2] L. Beltran-Sanchez, D.M. Stefanescu, Proceedings of the "Modelling of Casting, Welding, and Advanced Solidification Processes X", TMS, Destin, FL, USA, 2003, pp. 75–82
[3] A. Karma, W.J. Rappel, *Phys. Rev. E* **57** (1998) 4323-4349
[4] J.H. Jeong, N. Goldenfeld, J.A. Dantzig, *Phys. Rev. E* **64** (2001) 1-14
[5] M. Eshragi, S.D. Felicelli, B. Jelinek, *J. Crys. growth* **354** (2012) 129–134
[6] C.A. Gandin, M. Rappaz, *Acta Met.* **45** (1997) 2187-2195
[7] L. Nastac, 4th Pacific Rim International Conference on Modeling of Casting and Solidification Processes (MCSP-4), C.P. Hong ed., Yonsei University, Seoul, Korea, September 5-8, 1999
[8] L. Nastac, Proceedings of the "Modelling of Casting, Welding, and Advanced Solidification Processes IX", Engineering Foundation, Aachen, Germany, August 20-25, 2000

https://doi.org/10.1051/metal/2014016 Published online by Cambridge University Press

[9] L. Nastac, "Modeling and Simulation of Microstructure Evolution in Solidifying Alloys", Springer, New York, 2004
[10] L. Nastac, D.M. Stefanescu, Modelling and Simulation in Materials Science and Engineering, *Institute of Physics Publishing* **5** (1997) 391-420
[11] D.B. Kothe, R.C. Mjolsness, M.D. Torrey, RIPPLE: A Computer Program for Incompressible Flows with free surfaces, Los Alamos National Lab., LA-10612-MS, Los Alamos, NM, 1991
[12] S. Chen, B. Merriman, S. Osher, P. Smereka, *J. Comp. Phys.* **135** (1997) 8-29
[13] L. Nastac, D.M. Stefanescu, *Metal. Transact.* **28A** (1997) 1582-1587
[14] M. Kong, R.N. Bhattacharyal, C. James, A. Basu, *Geol. Soc. Am. Bull.* **117** (2005) 244-249

https://doi.org/10.1051/metal/2014016 Published online by Cambridge University Press